Finite Size Effects in Near Field Radiative Heat Transfer

by

Meher Dev Gudela

B.Eng., University of Mumbai, 2021

A thesis submitted to the

Faculty of the Graduate School of the

University of Colorado in partial fulfillment

of the requirements for the degree of

Master of Science

College of Engineering and Applied Sciences

2023

Committee Members:

Longji Cui, Chair

Prof. Rong Long

Prof. Todd Murray

Gudela, Meher Dev (M.S., Mechanical Engineering)

Finite Size Effects in Near Field Radiative Heat Transfer

Thesis directed by Prof. Longji Cui

Radiative heat transfer is an extremely important area of study as it is the only mode of heat transfer which can occur is the absence of a medium. When radiative heat transfer occurs at a distance d which is smaller than the characteristic wavelength of radiative heat transfer it has been extensively studied that the Stefan-Boltzmann law of radiative heat transfer cannot predict the heat flux between two bodies due quantum effects such as photon tunneling. Hence in the near field the radiative heat flux is several orders of magnitude greater than the corresponding black body radiation. This gives rise to extremely interesting applications of radiative heat transfer at the nanoscale and heat flux enhancement. Current analytical solutions to solve near field radiative heat transfer between two parallel plates overestimate the radiative heat flux between the two surfaces as the analytical solutions do not consider energy loss due to escaping electromagnetic waves. This is because the parallel surfaces are considered to be infinitely long when compared to the distance between the surfaces. But as science progresses and object sizes become smaller and smaller the assumption that surfaces are infinitely larger than the distance between them can no longer hold true. Therefore this thesis focuses on studying the near field radiative heat transfer between surfaces than can be considered finite sized and establish the difference between the analytical heat flux and simulated heat flux to establish these finite size effects and understand the energy loss due to finite sizes. In particular, this thesis studies the finite size effects due to change in length and width of the two parallel and change in gap size d between two surfaces. For analytical studies this thesis uses the semi-infinte parallel plane approach and uses a multiphysics software known as SCUFF-EM which uses the fluctuating surface current approach alongside boundary element method to calculate temperature independent generalized flux which can in turn be used to calculate the energy transfer between two surfaces.

Keywords: Radiative heat transfer, near field heat transfer, finite size effects, boundary element method

Dedication

This thesis is dedicated to my parents and my brother and their never ending support.

Acknowledgements

I want to express gratitude to Dr. Cui for affording me the privilege of working in his research lab over the past few years. Without his invaluable guidance on navigating the challenges of research, this thesis would not have been possible.

I would like to thank Mohammad Habibi, a PhD student in Dr. Cui's lab for his constant support and guidance in writing this thesis. I would also like to thank the amazing friends I made along my graduate school journey.

Finally, I would like to express my utmost gratitude to my family who have lended me their unconditional support throughout my graduate degree.

Contents

Chapter

Figures

Figure

Chapter 1

Introduction

Thermal Radiation is a phenomenon that occurs universally at all lengths at non-zero absolute temperatures. According to Stefan-Boltzmann law the radiative heat flux between two bodies is given by $\sigma(T_1^4$ - $T_2^4)$ where $\sigma = 5.6704$ x 10^{-8} W/m^2K also known as the Stefan-Boltzmann constant and T_1 and T_2 are the temperatures of the two bodies in the system. [3] This principle holds true under the condition that the space between the two objects (d) emitting or absorbing radiation is substantially greater than the characteristic wavelength of thermal radiation (λ_T), as determined by Wien's displacement law. Accordingg to Wien's displacement law the spectral radiance between black body surfaces peaks at λ_{peak} and is given by λ_{peak} = b/T where T is the absolute temperature and b is the Wien's displacement constant equal to 2898 μmK. At room temperature (T=300K) the characteristic wavelength is close to 10 μm. Research in this regime (d $>>\lambda_T$) is typically called far-field thermal radiation. The upper limit of far-field thermal radiation is defined by Planck's blackbody radiation law. Beyond this regime, in the near-field, it has been found that there exists a much larger radiative heat transfer, several orders of magnitude greater than that between two blackbodies.

The variation in the gap distance significantly influences the overall heat transfer process, and this effect is the result of two interconnected factors. The first factor pertains to wave interference and becomes noteworthy when the separation distance (d) is in proximity to, yet still greater than, the characteristic wavelength of thermal radiation (λ_T). In such situations, the exchange of radiant energy between two objects requires an examination that considers the wave-like properties of

energy propagation. When an electromagnetic wave is emitted from one medium and transmitted through the empty space between the two objects, it undergoes multiple reflections within this gap. The outcome of this wave interference can be either constructive or destructive, contingent upon the phase disparities between these reflected waves. [4]

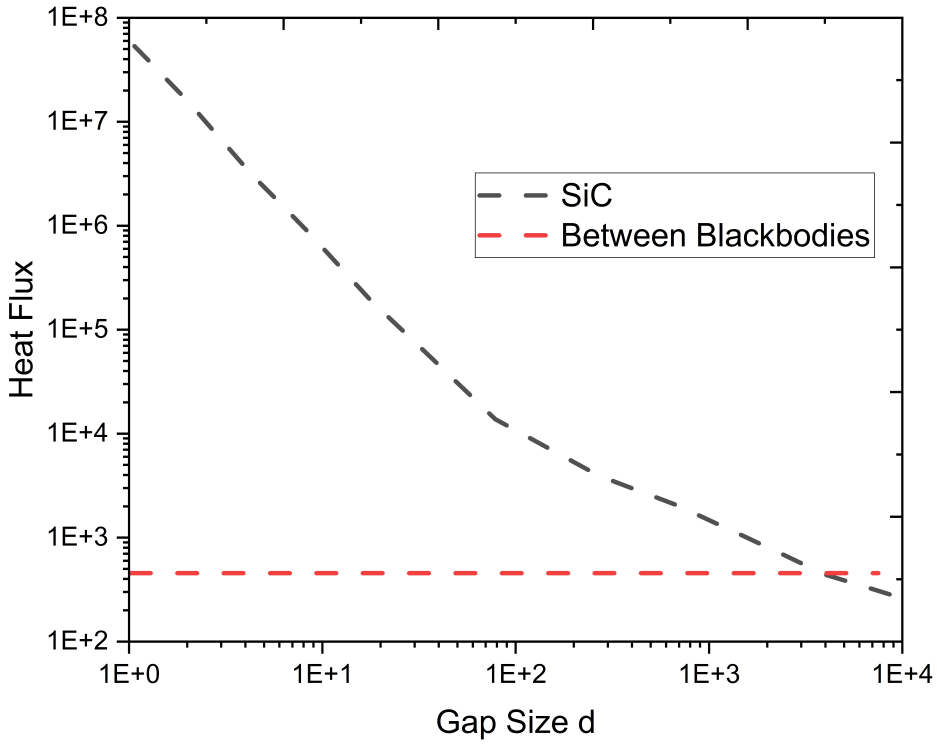

Figure 1.1: Near field radiative heat transfer between two SiC cubes compared to the energy transfer between two blackbodoes as a function of gap size d. [1]

The second factor associated with the gap distance is photon tunneling of evanescent waves, which assumes a substantial role in energy transfer in the near field when d is considerably smaller than λ_T. As an electromagnetic wave traverses through a medium and encounters a second medium with lower optical density, it undergoes total internal reflection at the interface if the angle of incidence surpasses a critical value. Despite being entirely reflected within the first medium, there exists an evanescent wave in the second medium that decays rapidly from the interface. This

evanescent wave, in contrast to the propagation wave which is responsible for radiative heat transfer in the far field and carries energy with it, does not convey energy in the normal direction because the time-averaged Poynting vector perpendicular to the interface is zero. [4]

If a third medium with a refractive index higher than that of the second medium is brought into proximity to the first medium, within the distance over which the evanescent wave diminishes, the evanescent wave reflects at the interface between the second and third media. The Poynting vector of the combined evanescent fields possesses a nonzero component in the normal direction, signifying that energy from the first medium has effectively traversed through the second medium and reached the third medium. This phenomenon is widely recognized as photon tunneling or radiation tunneling and serves as a fundamental mechanism for amplifying energy transfer in the near field. [4]

Rytov et. al. were the first to suggest a new way of looking at thermal radiation. They did this by combining the fluctuation-dissipation theorem with Maxwell's equations. This fresh approach changed how we study the heat radiation process. The fluctuation-dissipation theory equates fluctuating current densities which acts as a source for calculating thermal radiation with the temperature of the body. This helps us find the surface currents which in turn are used to calculate the generalized radiative flux which will be studied further in later chapters. [5] Pendry came up with the idea that wave vectors are like pathways that light follows when it travels. He also figured out a way to connect how much light bounces off and how much gets absorbed when two different materials meet. This is important for making near-field enhancement strong when it's very close to those materials. [6] Mulet et al. predicted that when you have dielectric materials that support surface phonon polaritons, the main factor influencing heat transfer in the nearby region is the contribution from surface waves. As a result, at extremely small distances, the flow of heat becomes nearly monochromatic. Surface phonon polaritons (SPhPs) are composite modes resulting from the interaction between electromagnetic waves and lattice vibrations (phonons) occurring at the surface of a material. These polaritons have the capability to travel along the boundary between two materials characterized by distinct dielectric properties. This interface commonly

involves a semiconductor or dielectric paired with an optical phonon-active substance, such as polar crystals or polar dielectrics. [7] Mulet et al. also investigated the close-range heat transfer between a particle, represented as a point-like dipole and an endless flat medium with a vacuum in between. Both the particle and the flat medium were assumed to be made of SiC material. The study's findings indicated that the near-field heat transfer grows proportionally to the cube of the separation distance, denoted as 'd', between the particle and the flat medium. [8] Rodriguez et al. discovered a new way to solve FSC approach for near field radiative heat transfer. This method was known as fluctuating surface current method in which the electric and magnetic surface currents are calculated first which are then used to calculate quantities of interest. First developed to calculate Casimir forces the FSC approach was later extended for near field radiative heat transfer. [9]

In this thesis we will study about the finite size effects in radiative near field heat transfer and compare our simulations with analytical models to estimate the overapproximation of heat flux due to the analytical models considering the surfaces of parallel plates to be infinitely long. We will compare the results for changing length and width of the surfaces as well as for changing gap size between the surfaces.

Chapter 2

Preliminaries

In this chapter we discuss the different methodologies available to solve Near Field Radiative Heat Transfer and introduce the finite size effects in near field heat transfer. In our work two different methods were used for the analytical solution and the simulated results respectively. The analytical solution to calculate NFHRT was done using MATLAB and the simulated results were done using an open-source Multiphysics software known as SCUFF-EM using the SCUFF-NEQ suite. The material covered in this chapter is only enough to understand the analytical and simulated results and should not be used as an introduction to the topics. There are several excellent books and research articles that are available online that serve as an introduction to NFHRT, and methods used to solve NFHRT.

2.1 Maxwell's Equations

When studying the interaction of heat radiation between solid objects, ray optics concepts are often applied to study the phenomenon as it occurs at their surfaces while considering the characteristics of the surfaces, such as their reflectivity, absorptivity, and emissivity. On the contrary, when addressing heat transfer through radiation within a semitransparent medium, researchers generally employ the radiative transfer equation. This equation considers the interplay of emission, absorption, and scattering phenomena within the medium. Under such a framework, near-field effects cannot be explained because the wave aspect of thermal radiation is disregarded in the radiative transfer equation. Maxwell's equations provide a comprehensive framework for describing

the behavior of electromagnetic waves and their interactions with material substances. Therefore, they should be utilized as the foundation for analyzing radiative heat transfer between closely positioned objects. Maxwell's equations for nonmagnetic media are given by: [10]

$$\nabla \times E(x,\omega) = i\omega\mu_0 H(x,\omega) = i\omega B(x,\omega) \tag{2.1}$$

$$\nabla \times H(x,\omega) = -i\omega\varepsilon E(x,\omega) \tag{2.2}$$

$$\nabla \cdot D(x,\omega) = \rho_e \tag{2.3}$$

$$\nabla \cdot B(x,\omega) = 0 \tag{2.4}$$

$$\nabla \cdot J(x,\omega) = i\omega\rho_e \tag{2.5}$$

Where,

E (V/m) - electric field

H (A/m) - magnetic field

D (C/m2) - electric displacement vector

B (Wb/m2) - magnetic flux density

J (A/m2) - electric current density

ρ_e (C/m3)- charge density

ε - permittivity of the medium

μ_0 - permeability of vacuum

Maxwell's equations can be solved using multiple methods that include both numerical and analytical solutions. The analytical solutions usually include green function formalism and thermal radiation in semi-infinite parallel plane systems. The numerical methods include the scattering matrix approach, fluctuating surface current approach, finite difference time domain method and wiener chaos expansion approach. Each method has their own pros and cons. [11] For the purposes of this thesis the thermal radiation in semi-infinite parallel plane system approach was modelled using MATLAB and for the simulated work using SCUFF-EM the fluctuating surface current

approach was used. The selection of method for the analytical part of the research was based on the ease of the method while considering the complexity of structures used in the analysis. Since most of our research was done using simple parallel plane surfaces such as two cubes placed parallel to each other the semi-infinite parallel plane system approach was the method that gave us the most accurate results that could be compared to the simulated results.

2.2 Semi-Infinite Parallel Plane Approach (Analytical Method)

The semi-infinite parallel plane approach was one of the first methods used to analytically solve near field heat transfer problems because of its simplicity. Carvalho et al. studied the spacing effect between two semi-infinite dielectrics that were kept at the temperature of liquid helium. This study established that the conventional heat transfer methods as stated by Stefan-Boltzmann law cannot be used at vacuum gaps that are less than or near to the characteristic wavelength. In this approach the total heat flux across a vacuum gap d is given by

$$q(T_1, T_2, d) = \int_0^\infty \frac{d\omega}{4\pi^2} \left[\Theta(\omega, T_1) - \Theta(\omega, T_2)\right] \int_0^\infty dkk \left[\tau_s(\omega, k) + \tau_p(\omega, k)\right] \tag{2.6}$$

Where $\Theta(\omega, T) = \frac{\hbar\omega}{e^{\frac{\hbar\omega}{kBT}}}$ also known as Bose-Einstein factor, is the mean energy of plank oscillator at frequency ω in thermal equilibrium which describes the spectral density of electromagnetic radiation emitted by a black body in thermal equilibrium at a given temperature T when there is no net flow of matter or energy between the body and its environment. The wave vector is denoted by k and τ_s and τ_p are the transmission probabilities for the TE and TM modes. In terms of Fresnel coefficients these are denoted as

$$\tau^{12}_{\alpha=s,p}(\omega, k) = \begin{cases} \dfrac{\left(1 - \left|r^{01}_\alpha\right|^2\right)\left(1 - \left|r^{02}_\alpha\right|^2\right)}{\left|D_\alpha\right|^2}, & k < \omega/c, propagating \\ \dfrac{4Im\left(r^{01}_\alpha\right) Im\left(r^{02}_\alpha\right) e^{-2Im\varsigma_2 d}}{\left|D_\alpha\right|^2}, & k > \omega/c, evanascent \end{cases} \tag{2.7}$$

The drawback of using this approach is that it is used only to calculate radiative heat transfer between thick objects and not thin films or layers. Systems with multiple layers of finite thickness cannot be calculated using this method because multiple emission sources and reflection cannot be

accounted for in multiple vacuum gaps using this method. Since our research does not focus on multi body systems or thin films the Semi-Infinite Parallel Plane Approach is an excellent way to analytically solve the radiative heat flux between a single emitter and receiver system. [12]

2.3 Fluctuating Surface Current Approach

Simulations for near field radiative heat transfer were done using an open-source Multiphysics software known as SCUFF-EM. While SCUFF-EM will be studied later in this thesis it is important to state the model SCUFF-EM uses to solve for NFRHT. Fluctuating surface current approach was formulated by Rodriguez et al. and is based on surface integral equation method. This approach is versatile in handling complex systems composed of diverse bodies, including those encapsulated within other structures. Moreover, it yields concise trace formulas for essential parameters, such as the emission from a solitary body or the radiative heat flux between multiple objects. These trace formulas facilitate a clear demonstration of thermal radiation. Additionally, it allows for the incorporation of the environmental contribution to radiative heat transfer. The FSC approach is expressed in terms of electric and magnetic currents that are not explicitly known but are present on the surfaces of the objects. [9] Given that the currents exclusively exist on the surfaces, employing the Boundary Element Method (BEM) with a surface discretization approach becomes feasible. This has the potential to decrease the quantity of unknowns that need to be resolved, making the FSC approach an attractive choice, especially for intricate systems. The equations used by SCUFF-EM to solve for surface currents will be studied in the next chapter of this thesis.

2.4 Finite Size Effects

Within the realm of radiative heat transfer, finite size effects assume an important role. When investigating heat transfer between objects at distances smaller than the wavelength of thermal radiation, the finite physical dimensions of these objects introduce variations in crucial radiative properties, such as emissivity and absorptivity. These variations exert a notable influence on the overall heat transfer dynamics. They result from the interplay of electromagnetic and thermal

radiation with small structures and closely spaced bodies, leading to deviations from classical predictions. In the far field (d $>>\lambda_T$) the finite size effects are akin to the view factor used in radiative heat transfer calculations. The view factor, is a dimensionless parameter that signifies the proportion of radiation emitted from the surface of one object that is captured by another object. In simpler terms, it measures the amount of radiation from one surface that reaches another surface in a thermal context. The view factor is denoted by the symbol F_{ij} where i and j are the surfaces and view factor is the ratio of radiation leaving i and reaching surface j. In near field analytical models such as the semi-infinite parallel plane model consider the two boundary surfaces to be infinite when compared to the distance between the two surfaces. Consequently, prevailing analytical models operate under the assumption that there are no energy losses associated with infinitely extended surfaces, and there is no leakage of electromagnetic waves. As science progresses and object sizes get smaller and smaller and the surface dimensions get closer to the distance between the surface analytical solutions considering infinite surfaces cannot hold true. Therefore, it is important to study the finite size effects that occur when the dimension of two parallel surfaces happen to be closer to the distance of the two finite surfaces. Since current analytical solutions can overestimate the approximate heat flux between two finite surfaces it is important to establish a theoretical approximation of actual heat flux which in turn can be used to accurately find values required to design nanostructures and devices. This thesis provides a clear picture of finite size effects in near field heat transfer and how the finite size effects vary when the dimensions of the objects are changed in terms of length and width and also when the gap size changes.

Chapter 3

Methodology

In this chapter we will provide an insight into SCUFF-EM and SCUFF-NEQ suite used to calculate non-equilibrium heat flux using the fluctuating surface current approach and integrating it with boundary element method. The chapter includes the modelling steps taken to model our systems. SCUFF-EM was installed and used on the Alpine Supercomputer that is provided and maintained by CU Research Computing.

3.1 SCUFF-EM

SCUFF-EM is an open-source Multiphysics software created by Dr. Homer Reid during his time at MiT. It uses a method known as boundary element method to model fluctuation induced electromagnetic phenomena. This includes solving for casimir forces and radiative heat transfer. SCUFF-EM stands for **S**urface **CU**rrent **F**ield **F**ormulation of **E**lectro**M**agnetism which refers to the numerical solution used by SCUFF-EM called fluctuating surface current approach (FSC) which was discussed in the previous chapter. FSC approach is combined with boundary element method to first find both electric and magnetic currents on the surface interfaces between mediums. Using the electric and magnetic surface currents it is possible for SCUFF-EM quantities of interest which in our case is the temperature independent generalized flux. Since electric and magnetic currents are considered to only occur at boundaries, the boundary element method acts as a great alternative to the more commonly used finite element method as SCUFF-EM doesn't require to discretize an entire geometry and can work by only discretizing the boundaries of the system.

This reduces the computational power required to run finer meshes to achieve accurate results. On the other hand, in contrast to finite-element and finite-difference approaches, BEM typically produces dense matrices that necessitate extensive matrix operations, hence increasing computing complexity and time. Since our work does not require complex geometries SCUFF-EM acts as the perfect simulation tool to calculate the temperature independent generalized flux. [13]

3.1.1 Boundary Element Method

The Boundary Element Method (BEM) represents a highly potent computational tool where, in contrast to discretizing the entire domain, emphasis is placed solely on discretizing the domain's boundary. Owing to its efficiency and unique problem-solving approach, BEM has evolved into a pivotal instrument for addressing a spectrum of engineering and multiphysics challenges. The fundamental principle of BEM involves simplifying complex physical problems by concentrating on the boundary, formulating integral equations aligned with governing physical principles. These equations establish connections among pertinent values along the boundary, resulting in a system of equations that encapsulates the problem's core aspects. This distinctive methodology provides BEM with a pronounced advantage, particularly in scenarios where the solution exhibits variations primarily along the boundary.

Traditional methods, such as the Finite Element Method (FEM), often grapple with computational demands arising from the analysis of the entire domain. In contrast, BEM, with its boundary-centric focus, frequently exhibits advantageous traits, especially when the solution varies predominantly along the boundary. The reduction in dimensionality inherent in the boundary-centric approach has the potential to yield a reduced system of equations, thereby enhancing computational efficiency. BEM's ability to streamline calculations to the boundary surfaces diminishes the need for extensive computational power, presenting itself as an efficient alternative to FEM, especially in electromagnetic wave calculations using the fluctuating-surface current (FSC) method.

In the discretization process of BEM, the boundary is partitioned into smaller elements, each associated with unknowns representing values of interest. These elements serve as the basis for craft-

ing integral equations, laying the groundwork for employing diverse numerical techniques to solve the ensuing system of equations. BEM's prominence extends into the realm of electromagnetics, where it proves instrumental in studying phenomena induced by electromagnetic fluctuations. Its applications range from computing rates for radiative heat transfer to determining non-equilibrium Casimir forces and torques, accommodating bodies with diverse shapes and material properties. BEM's adaptability in addressing challenges related to varying permittivity and permeability in distinct boundary regions underscores its versatility in electromagnetics applications.

As a sophisticated and effective numerical strategy, BEM stands out in scenarios where the solution predominantly varies along the boundary. Its distinctive approaches to discretization, dimensionality reduction, and singularity handling position it as an invaluable tool for exploring diverse physical phenomena. As computational capabilities continue to advance, BEM maintains its pivotal role in the numerical toolkit, providing engineers and researchers with a reliable means to achieve precise and efficient solutions for intricate problems. [14]

3.1.2 SCUFF-NEQ

Scuff-neq plays a pivotal role in the comprehensive scuff-em software suite, specifically tailored for the exploration of non-equilibrium (NEQ) electromagnetic fluctuations. Its primary objective is to analyze rates associated with radiative heat transfer, non-equilibrium Casimir forces, and torques across diverse shapes characterized by varying frequency-dependent permittivity and permeability—exhibiting linearity, isotropy, and piecewise homogeneity. Utilizing the fluctuating-surface current (FSC) method, scuff-neq engages in numerical simulations tailored for non-equilibrium fluctuation phenomena. Originating as a tool primarily focused on equilibrium Casimir forces, it underwent enhancements to proficiently handle non-equilibrium scenarios, such as radiative heat transfer, demonstrating versatility in addressing an array of non-equilibrium forces and torques.

An inherent feature of scuff-neq lies in its ability to compute temperature-independent parameters known as generalized fluxes. These fluxes provide a nuanced understanding by delineating contributions from different frequencies within the domain of fluctuating electromagnetism. Cate-

gorized into spatially integrated (SI) measures, encompassing overall rates like heat absorption or emission, total force, or torque, and spatially-resolved (SR) measures, delving into specifics like the Poynting flux or the Maxwell stress tensor at specific locations.

Following its calculations, scuff-neq generates data files storing the values of generalized fluxes at specified frequencies, offering a detailed perspective on the system's behavior under diverse electromagnetic conditions. Subsequently, the companion utility, scuff-integrate, undertakes the task of post-processing, computing average values for both spatially integrated (SI) and spatially-resolved (SR) quantities across a range of temperatures. In essence, scuff-neq serves as a valuable tool for researchers seeking insights into heat transfer and forces within electromagnetic systems operating in non-equilibrium states. Its evolution from studying equilibrium Casimir forces to handling more intricate scenarios underscores its adaptability. The method's capability to calculate temperature-independent values, coupled with the subsequent analysis through scuff-integrate, contributes significantly to understanding these phenomena across varying temperatures.

Consider a system of bodies of homogeneous material kept in equilibrium. The bodies are maintained at a constant temperature in a vacuum filled environment. The bodies carry thermal induced electromagnetic fields due to the presence of fluctuating surface electric and magnetic currents. The electromagnetic field radiated from the body due to these currents carry both energy and momentum which can be split into two terms: (a) spatially integrated terms such as heat flux absorbed or radiated by the body or and (b) spatially resolved quantities which can be the poynting vector or maxwell stress tensor at certain points in space. According to the FSC approach the value of total radiated energy is given by the sum of all the contributions from all bodies due to fluctuating currents.

$$\langle Q \rangle = \int_0^\infty \sum_b \Theta\left(T_b, \omega\right) \Phi_b\left(\omega\right) d\omega \tag{3.1}$$

$$\Theta\left(T_b, \omega\right) = \frac{\hbar\omega}{e^{\frac{\hbar\omega}{kT_b}} - 1} \tag{3.2}$$

$$\langle Q \rangle = \langle Q \rangle^{EQ} + \langle Q \rangle^{NEQ} \tag{3.3}$$

$$\langle Q \rangle^{EQ} = \int_0^\infty \Theta\left(T_{env}, \omega\right) \sum_b \Phi_b\left(\omega\right) d\omega \tag{3.4}$$

$$\langle Q \rangle^{NEQ} = \int_0^\infty \sum_b \left[\Theta\left(T_b, \omega\right) - \Theta\left(T_{env}, \omega\right)\right] \Phi_b\left(\omega\right) d\omega \tag{3.5}$$

where T_b is the temperature of body b and $\Phi_b(\omega)$ is a quantity solved by scuff-neq known as the temperature-independent generalized flux describing the contribution of frequency ω source fluctuations in body b. $\Theta(T_b,\omega)$ is the bose einstein factor where where $\hbar$ is the Planck constant divided by 2π, k is the Boltzmann constant, and T is the absolute temperature of the source medium. It relates the temperature of the body to the nature of the current density vector related to the specific wavelength specified.

Q^{EQ} and Q^{NEQ} are the thermal equilibrium heat flux and non-equilibrium heat flux described in the system. Q^{NEQ} is the average value of Q if all the bodies in the system are kept at the exact same temperature as the environment the system is in. If Q is a spatially integrated power transfer quantity, then the value of Q^{EQ} is zero and hence not calculated by scuff-neq. In other cases Q^{EQ} can be calculated using resources that are much less intensive than scuff-neq such as basic theoretical equations. Since our work relies on the non-equilibrium nature of the system we only need to calculate the Q^{NEQ} part of the equation where SCUFF-NEQ calculates the temperature independent generalized heat flux which in turn needs to be substituted in the integral form to get the final value of Q^{NEQ}. These values are summed over b where b is the number of bodies in the system. [13]

3.2 Modelling for SCUFF-EM

SCUFF-EM is an entirely text-based program that does not have a GUI for the user to interact with. This makes using SCUFF-EM for simulations a bit more complicated to use than other Multiphysics simulation tools such as COMSOL which is widely used for Multiphysics simulations. In this section we will go through the process of modelling structures using text-based commands required to run SCUFF-EM.

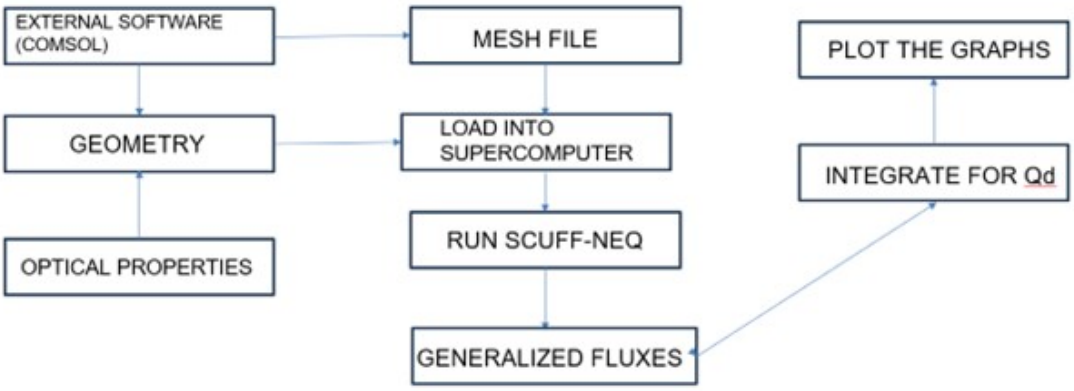

Figure 3.1: A flowchart showing the process of modeling for simulations on SCUFF-EM

3.2.1 Geometric Modelling

SCUFF-EM itself has no inbuilt 3D modelling suites like the one given in COMSOL. Hence it depends on external modelling softwares to create structures and mesh the geometries. These geometries can in turn be converted into text-based files which can then be used as an input to run SCUFF-EM and SCUFF-NEQ simulations. SCUFF-EM allows geometric modelling through two softwares: (a) GMSH and (b) COMSOL. The 3D geometry files obtained from these softwares can be converted to text-based mesh files using. msh extension (from GMSH) and. mphtxt extension (from COMSOL). Based on convenience and a better GUI the author decided to COMSOL as the primary modelling and meshing tool.

To model on COMSOL you can make use of the in-built model builder that is integrated in the COMSOL application. Since SCUFF-EM uses default unit length as micrometers it is important to model geometries in COMSOL in with the length units set to micrometers (um). For example, if you're simulating the radiative heat flux of a cube with dimensions 100nm x 100nm x 100nm, in COMSOL you would model the cube using the dimensions 0.1μm x 0.1μm x 0.1μm.

After modeling the geometry, the next step is to mesh the cube. On COMSOL there are two types of meshing features. (a) User defined mesh and (b) Physics defined mesh. Since our

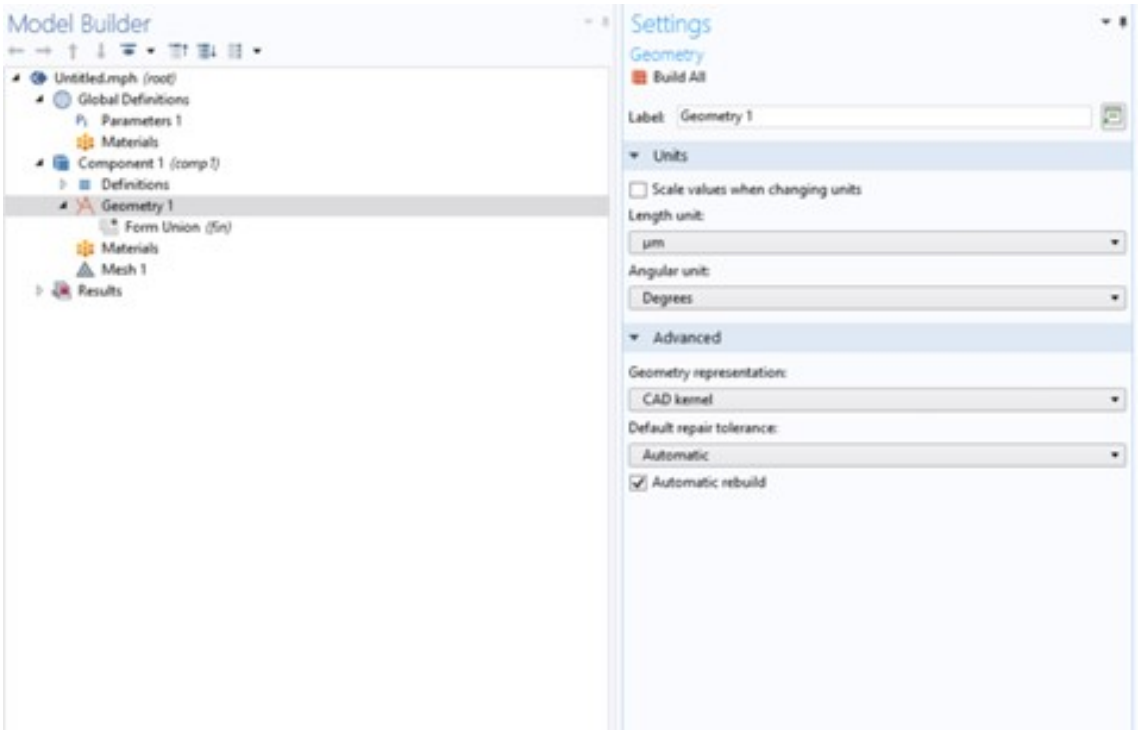

Figure 3.2: GUI of COMSOL and setting the length unit to μm

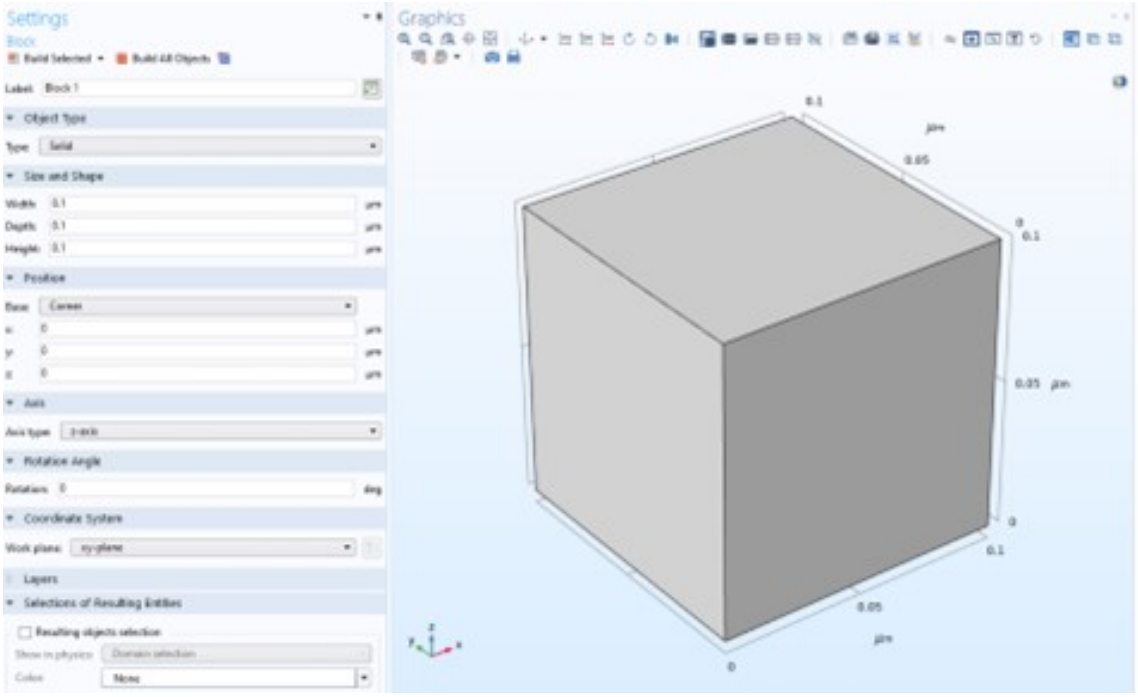

Figure 3.3: Modeling a 0.1μm x 0.1μm x 0.1μm cube on COMSOL

simulations are not dependent on the physics-based boundary conditions in COMSOL we used user-defined mesh as it suited our needs better. COMSOL exhibits adaptive meshing capabilities, enabling real-time refinement of the mesh throughout the simulation in response to the evolving solution behavior. This dynamic adaptability ensures the efficient allocation of computational resources to regions of particular interest. The mesh is refined in areas requiring heightened accuracy while being coarsened in others to optimize computational efficiency. This adaptive meshing approach enhances the precision of simulations by strategically managing computational resources in accordance with the evolving characteristics of the solution. COMSOL has a wide range of element types to choose from based on the geometry of the model and the physics of the simulation. These include triangular, quadrilateral, tetrahedral, hexahedral, and prismatic elements. Different elements offer advantages in terms of computational efficiency and solution accuracy for specific types of simulations. For our simulations we used free triangular elements since they provided us with accuracy and reduced the need for higher computational resources.

Once the model is prepared with all the necessary components, we can access the "File" menu and choose the "Export" option. Selecting the .mphtxt file format and specifying the desired save location initiates the export process. The resulting .mphtxt file, being in plain text, is easily readable and editable using any text editor, facilitating transparency in understanding the model's structure and parameters. Since SCUFF-EM requires text based inputs for mesh files .mphtxt files act as an excellent option to have as you can import them back to COMSOL to get a visual representation of the created model.

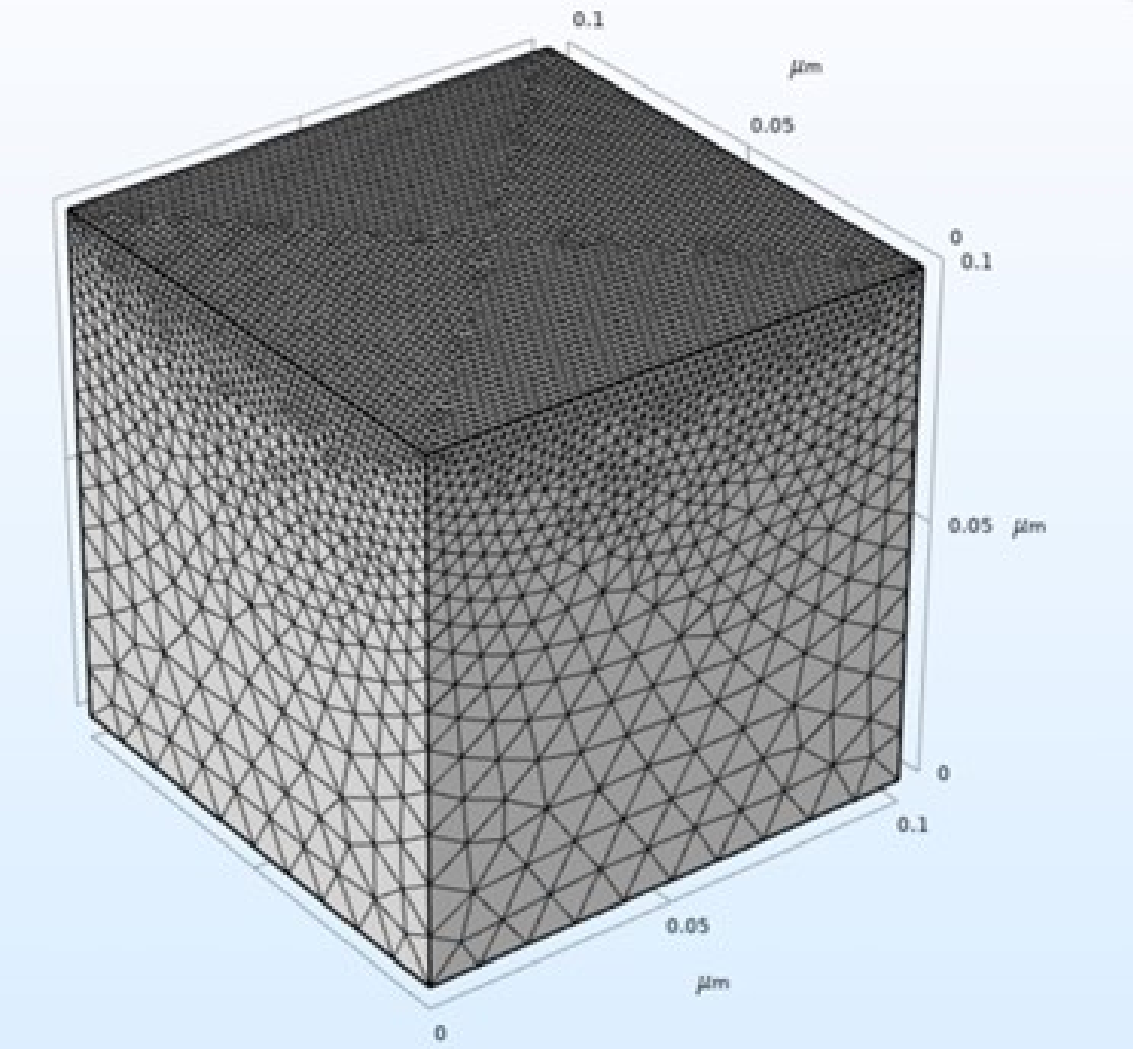

Figure 3.4: Meshing a 0.1μm x 0.1μm x 0.1μm cube on COMSOL. The top domain was meshed with the fine mesh settings while the rest of the geometry was meshed with the coarse mesh settings. The mesh growth rate was kept at 1.1 for a smoother transition from fine mesh to coarse mesh.

3.2.2 SCUFFGEO Files

As stated SCUFF-EM only accepts text-based inputs to run simulations. The geometries in SCUFF-EM are described solely by text files with .SCUFFGEO extensions. SCUFFGEO files include the material designations, optical/electrical properties, links to the mesh file created on COMSOL and geometric transformations of the geometries linked through the mesh files. .SCUFFGEO files assign material properties such as dielectric permittivity and magnetic permeability

through built-in materials or user defined materials. Built-in materials have dielectric functions of the materials pre-loaded into SCUFF-EM and therefore only need to be mentioned in the .SCUFF-GEO file without any added data. Built-in materials in SCUFF-EM include PEC or Vacuum. User defined materials need to be specified with a dielectric function. For example to assign a geometry with the material Silicon Carbide the designation in the .SCUFFGEO file will look something like this:

MATERIAL SiliconCarbide

EpsInf = 6.7;

a0 = -3.32377e28;

a1 = +8.93329e11;

b0 = -2.21677e28;

b1 = 8.93329e11;

Eps(w) = EpsInf * (w2 + a1*i*w + a0) / (w2 + b1*i*w + b0);

ENDMATERIAL

The first line defines the name of the material. The constant values when substituted in the Eps(w) equation give the relative permittivity of the material which is expressed as function of frequency ω. "i" in the equation expresses the presence of the imaginary number. After the material is defined in the .SCUFFGEO file the next step is to link the mesh file created in COMSOL to the .SCUFFGEO file to assign the mesh file the specified materials. Each object present in the simulation needs to be assigned a name for SCUFF-EM to refer to. For example, using the mesh file created previously in this thesis, named block1.mphtxt, and assigning the material Silicon Carbide that we defined above:

MATERIAL SiliconCarbide

EpsInf = 6.7;

a0 = -3.32377e28;

a1 = +8.93329e11;

b0 = -2.21677e28;

b1 = 8.93329e11;

Eps(w) = EpsInf * (w2 + a1*i*w + a0) / (w2 + b1*i*w + b0);

ENDMATERIAL

OBJECT s1

MESHFILE block1.mphtxt

MATERIAL SiliconCarbide

ENDOBJECT

We have now successfully created a geometric file and have assigned the material Silicon Carbide to the geometry that was made on COMSOL.

3.2.3 Running SCUFF-NEQ Simulation

Although BEM reduces the amount of computational power needed to run the simulations, SCUFF-NEQ simulations still require considerable amount of computational resources as the number of matrices required to solve increases as the fineness of the mesh increases. With the available hardware of the author limited 64GB of RAM and an Intel I7 processor it was essential to find an alternative to solve the need for higher computing power. Therefore Alpine Supercomputer was chosen. Alpine serves as the University of Colorado Boulder Research Computing's advanced high-performance computing (HPC) cluster, representing its third-generation infrastructure. This heterogeneous compute cluster is assembled with hardware contributions from the University of Colorado Boulder, Colorado State University, and Anschutz Medical Campus. Currently boasting 382 compute nodes and a cumulative core count of 22,180, Alpine stands as a robust computing resource. Accessible securely from any location and at any time, users can utilize Open OnDemand or SSH connectivity to connect to the CURC system. Notably, all nodes within Alpine are universally available to all users, enhancing its inclusivity and usability for diverse research endeavors. SCUFF-EM was installed on Alpine on a global level for any user from CU Boulder, CU Anschutz and Colorado State University to use it for free. To run SCUFF-NEQ the author used the batch queue command on Alpine. This allowed the author to queue up multiple simulations at once and

hence reducing the overall wait time to run the simulations. The code to run a simulation with the created mesh files and .SCUFFGEO file is given below.

!/bin/bash

SBATCH –partition=amilan

SBATCH –nodes=1

SBATCH –ntasks=64

SBATCH –time=10:00:00

ml purge

ml singularity/3.7.4

in case of threading

export SINGULARITYENVOMPNUMTHREADS=SLURMNTASKS

singularity exec –bind /scratch/alpine CURCCONTAINERDIR/scuff-em-jfeist.sif scuff-neq –geometry block.SCUFFGEO –OmegaValues 0.3

This line of code is conveying to the supercomputer to run the block.SCUFFGEO file with a frequency of 0.3*3.14e14 rad/sec and give an output of temperature independent generalized fluxes.

3.3 Validation

Before we can start simulating our geometries to find the generalized flux through SCUFF-NEQ, it is important to validate any results that we may have to set up the accuracy of our simulations. K.L. Nguyen et al. [2] calculated both the theoretical and numerical values of radiated power for two cases. The first case was for a single Silicon Carbide sphere of radius 0.1um and the second case was for two Silicon Carbide spheres at temperatures T1 and T2 respectively. The radius of these spheres are 0.1um and the distance between the two SIC spheres was chosen to be 10um.

3.3.1 Thermal emission for a single SIC sphere

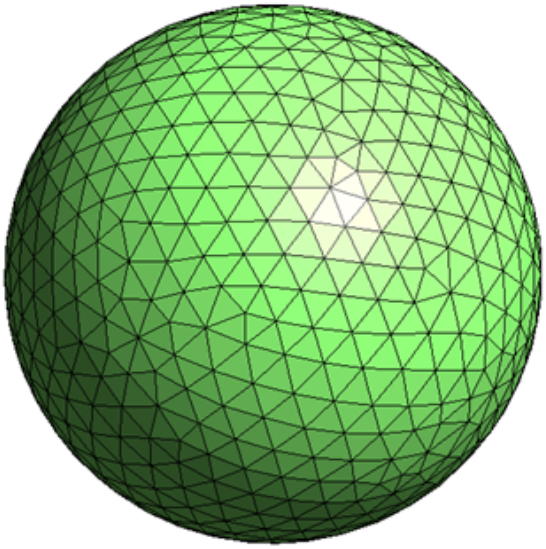

Figure 3.5: Mesh geometry of a single SIC sphere

To validate our results, we first run the single SIC sphere case. To ensure that the simulated geometries are similar to the ones used in K.L. Nguyen et al. [2] we used the dielectric function given by the authors which is $\epsilon(\omega) = \epsilon_\infty \left(1 + \frac{\omega_L^2 - \omega_T^2}{\omega_T^2 - \omega^2 - i\Gamma\omega}\right)$ where ϵ_∞=6.7 ω_L=1.825 x 10^{14} rad/sec ω_T=1.494 x 10^{14} rad/sec Γ=8.966 x 10^{11} rad/sec

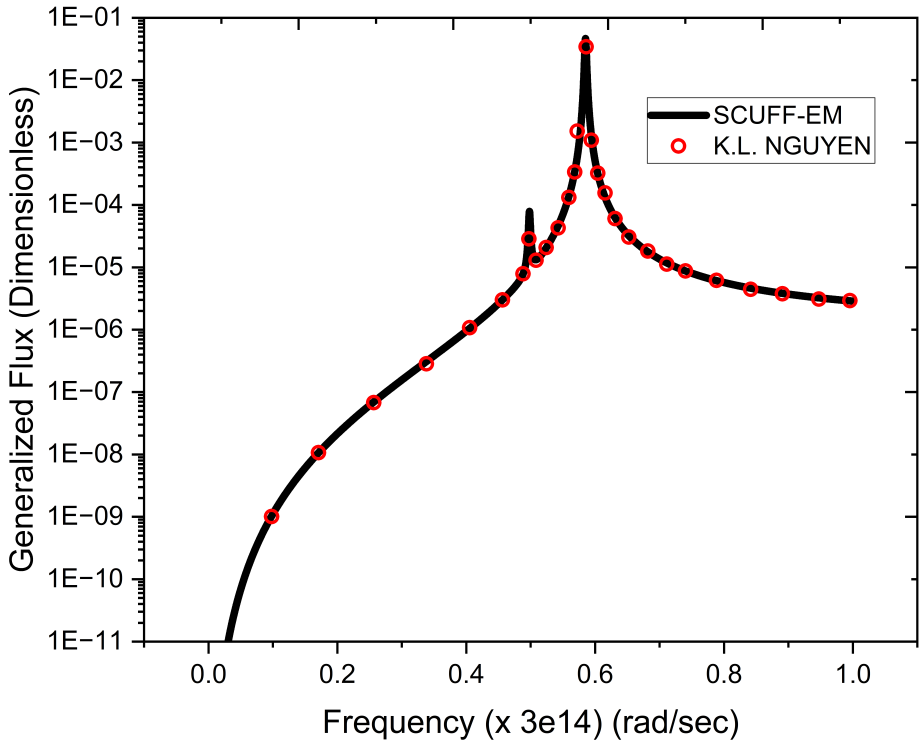

Figure 3.6: Generalized flux for a single SiC sphere of radius 0.1 μm. Black line indicates the simulated values through SCUFF-EM and red circles indicate the values taken from K.L. Nguyen et al. [2]

The sphere was meshed using free triangular elements on COMSOL. The mesh element size was chosen to be 0.017um to keep the mesh geometry similar to the ones used in K.L. Nguyen et al. [2] The simulation was ran at a frequency range of 0.1 x 10^{14} rad/sec to 3 x 10^{14} rad/sec.

3.3.2 Thermal transfer for two SIC spheres

The next model we used to validate our results was to calculate the radiated flux between two Silicon Carbide spheres. The spheres were modeled to be 0.1 um each with a 10um gap between them. The mesh geometry was kept the same as the one used for the single sphere case. Similar to the first case the dielectric function used was $\epsilon(\omega) = \epsilon_\infty \left(1 + \frac{\omega_L^2 - \omega_T^2}{\omega_T^2 - \omega^2 - i\Gamma\omega}\right)$ where ϵ_∞=6.7 ω_L=1.825

x 10^{14} rad/sec ω_T=1.494 x 10^{14} rad/sec Γ=8.966 x 10^{11} rad/sec [2]

The black line indicates the simulated values, and the red circles indicate the values obtained from K.L Nguyen et. al. The generalized flux peaked at frequencies 1.5 x 10^{14} rad/sec and 1.75 x 10^{14} rad/sec which are the resonant frequencies for SIC. The figure represents the generalized flux from sphere 1 to sphere 2 which were kept 10 μm apart.

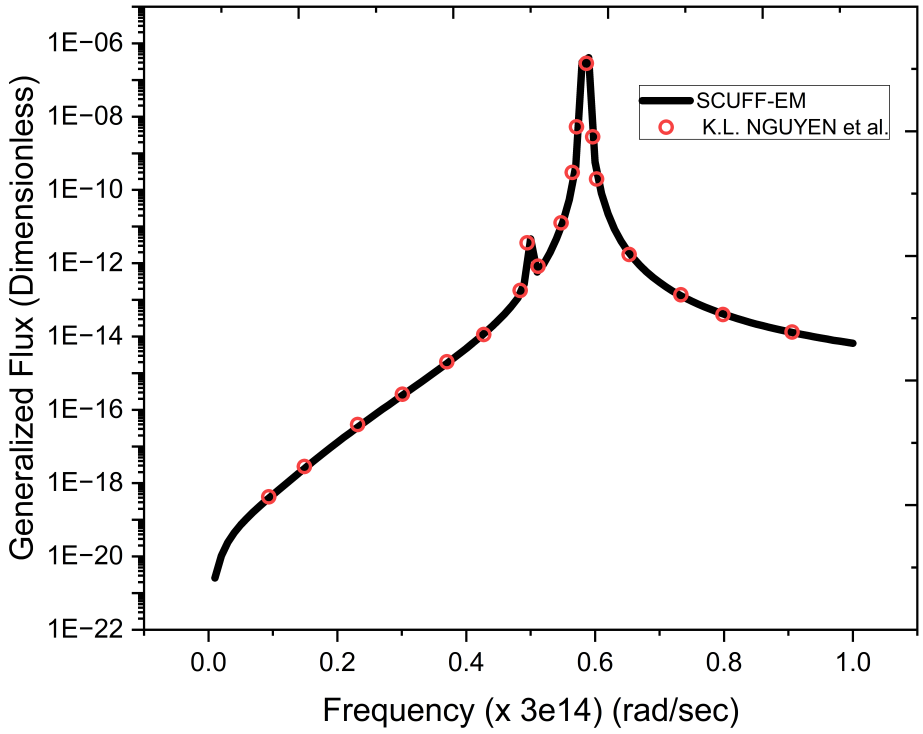

Figure 3.7: Generalized flux for a two SiC spheres of radius 0.1 μm and center to center distance of 10 μm. Black line indicates the simulated values through SCUFF-EM and red circles indicate the values taken from K.L. Nguyen et al. [2]

As shown in the figures our results perfectly align with the results computed by Nguyen et al. This serves as the validation required to move forward in our work.

Chapter 4

Results

In this chapter we will discuss the simulated results of the generalized flux obtained from SCUFF-NEQ. After going through the results well compare the results with the analytical results that we obtained using the semi-infinite parallel plane method. Lastly, we will plot the obtained Q from the generalized flux calculated against the change in length and width and change in the gap size between the surfaces.

4.1 Mesh Independence

The exploration of mesh independence is extremely significant for numerical simulations, particularly in methods such as the boundary element method and finite element method. This involves a meticulous examination of the impact of mesh size on simulation outcomes. The primary objective is to ascertain that the numerical solution converges to a stable and accurate state as the mesh undergoes refinement. In the mesh independence study, we're trying to make sure that our simulation results are dependable and resilient. We do this by carefully looking at how the solution changes when we use different levels of mesh detail. The main idea is that as we make the mesh more detailed, the simulation should give us a stable and consistent result, showing that it's not overly dependent on specific mesh settings. For the mesh independence study, we selected the case of 50nm x 50nm x 50nm Au cubes which were placed at a gap of 5nm between them. The top boundary of the bottom cube and the bottom boundary of the cube placed 5nm above the first cube are meshed from a range of coarse mesh to fine mesh. The rest of the boundaries

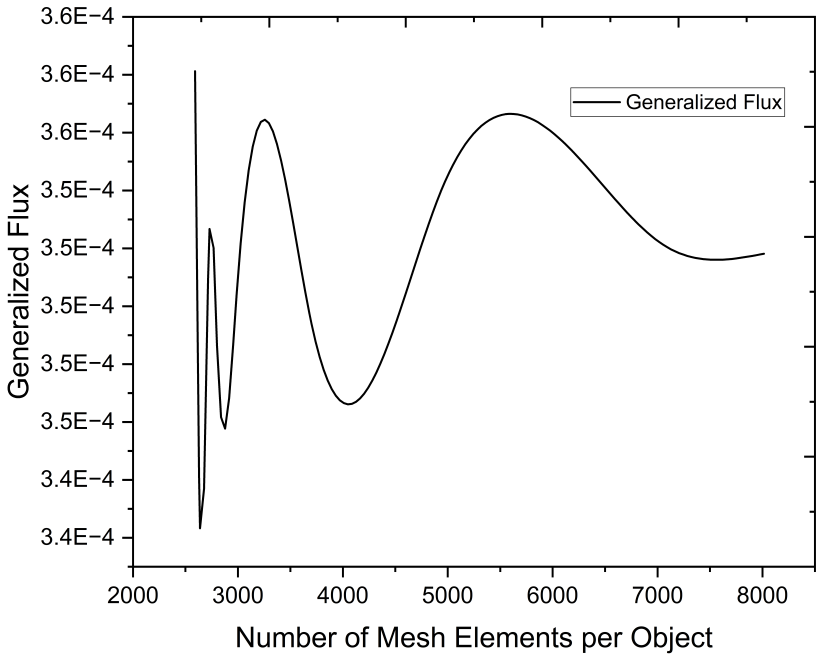

(a) Varying Generalized Flux between two gold cubes of 50nm x 50nm x 50nm with a gap of 5nm for increasing number of mesh elements.

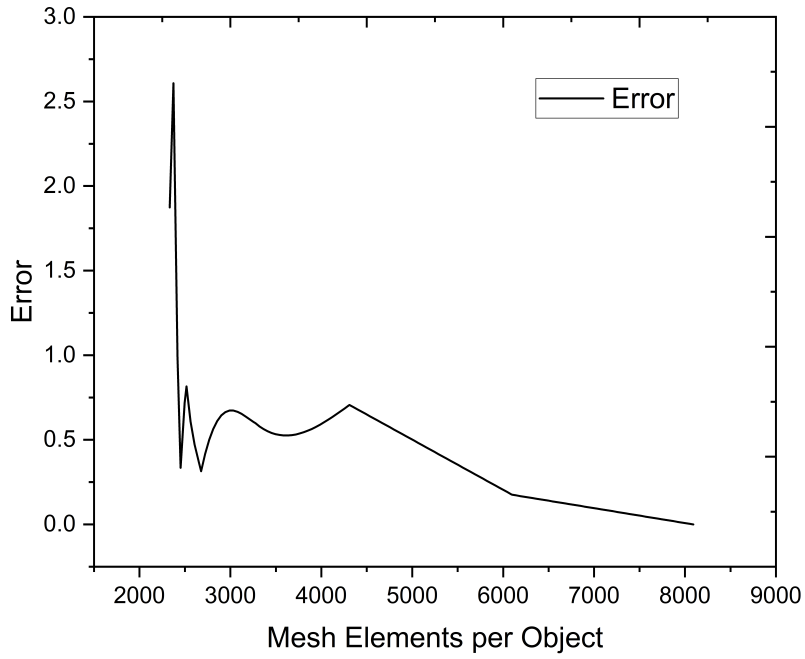

(b) Error vs. Mesh Elements

Figure 4.1: Mesh independence study two gold cubes of 50nm x 50nm x 50nm with a gap of 5nm

of both the cubes are kept at normal mesh settings. Both cubes are meshed similarly to make the mesh independence study easier. The mesh element growth rate was kept slow at 1.1 to make the transition from the fine or coarse mesh to the normal mesh smoother. The meshing of the cubes was done on COMSOL and SCUFF-NEQ simulations were done on Alpine Supercomputer. The dielectric function used to define the material Au was given as $\epsilon(\omega) = \frac{(1-\omega_p^2)}{\omega(\omega+i\Gamma)}$ where ω_p=1.37 x 10^{16} and Γ=5.32 x 10^{13} SCUFF-EM could only handle mesh elements upto 8000 boundary elements per cube due to the exorbitant amounts of computational power needed to go beyond that. Hence, we chose a range from 2000 elements to 8000 elements. Even upto 8000 elements the system was seen to be sensitive to the change in mesh elements. Due to this we decided to run our simulations at the maximum number of mesh elements that we could at the computational power available to us. For 8000 mesh elements SCUFF-EM used up 217GB of RAM and took 26 minutes to solve for the generalized flux at each frequency ω that was specified. SCUFF-EM could only handle mesh elements upto 8000 boundary elements per cube due to the exorbitant amounts of computational power needed to go beyond that. Hence, we chose a range from 2000 elements to 8000 elements.

4.2 Simulated vs Analytical Results for changing length and width of the cube

Now that we have validated our results from SCUFF-EM and performed a mesh independence analysis we can move forward to discuss the results. As stated before, the analytical results were calculated using MATLAB and the semi-infinite parallel plane method and the simulated results were done on the SCUFF-NEQ suite of SCUFF-EM. For the changing length and width analysis of fine size effects we considered three cases. All three cases were similar to the geometry used in the mesh independence study. The length and width of the cube were changed while the height of the cube was kept at 50nm. The gap size between the cubes was kept at 5nm. The dielectric function, delineating the material properties of gold (Au), was incorporated into the simulations which was given by $\epsilon(\omega) = \frac{(1-\omega_p^2)}{\omega(\omega+i\Gamma)}$ where ω_p=1.37 x 10^{16} and Γ=5.32 x 10^{13}

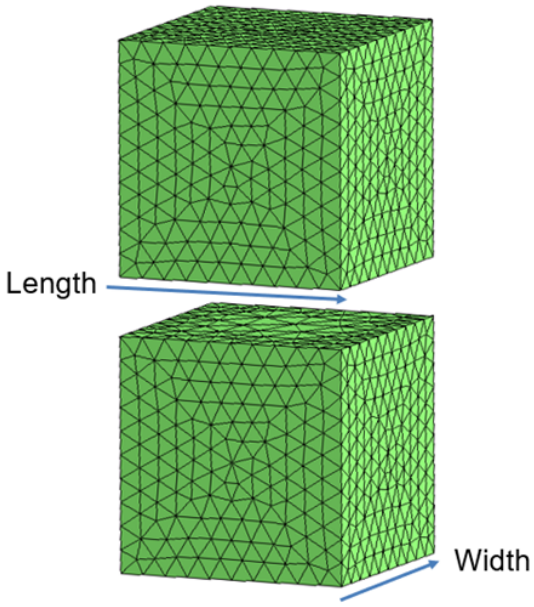

Figure 4.2: Visualization of changing length and width between two cube geometries.

4.2.1 20nm x 20nm x 50nm Au Cubes

The initial simulation involved 20nm x 20nm x 50nm gold cubes positioned with a 5nm separation. The top boundary of the lower cube and the bottom boundary of the cube positioned 5nm above were finely meshed to enhance result accuracy, while the remaining boundaries were set to normal mesh settings due to their minimal impact on calculating the generalized flux. Uniform meshing of both cubes aimed at simplifying the simulation and facilitating analytical method solutions. A slow mesh element growth rate of 1.1 was employed for smoother transitions between fine and normal mesh regions. The meshing process was conducted using COMSOL, and SCUFF-NEQ simulations were executed on the Alpine Supercomputer. The surface plasmon resonance of gold nanocubes was observed within the frequency range of 0.2 x 3e14 rad/sec to 0.3 x 3e14 rad/sec, as evidenced by peaks in both analytical and simulated results. The red line represents the analytical solution for the generalized flux, while the black line signifies the simulated results. The alignment of peaks at identical frequencies suggests the accuracy of the simulated outcomes. Discrepancies in

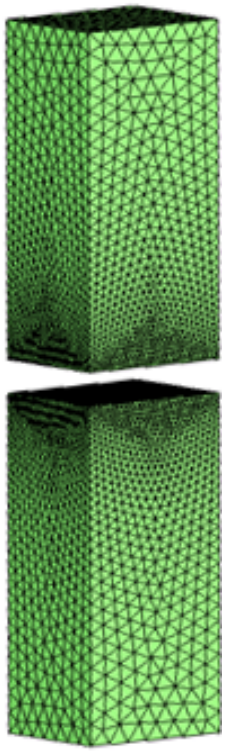

(a) Mesh geometry of 20nm x 20nm x 50nm Au Cubes with a gap of 5nm.

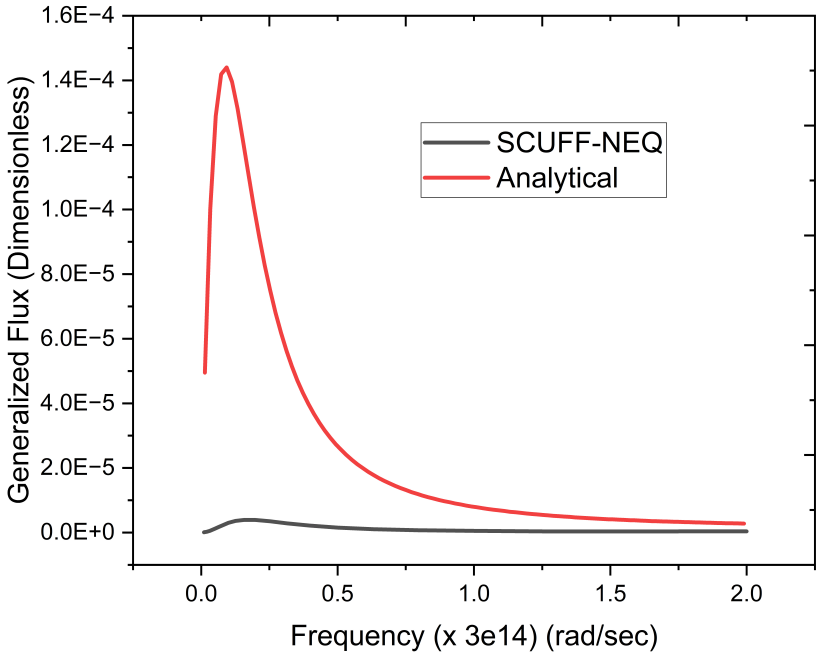

(b) Generalized Flux vs. Frequency for 20nm x 20nm x 50nm Au Cubes with a gap of 5nm.

Figure 4.3: Comparing values of generalized flux using analytical method and SCUFF-EM simulations for 20nm x 20nm x 50nm Au Cubes with a gap of 5nm.

the peak values of the generalized flux point to the analytical solutions overestimating energy transfer between the boundaries, attributed to the oversight of escaping electromagnetic waves. This observation underscores the presence of finite size effects, particularly relevant given the proximity of the boundary sizes to the gap between the two objects.

4.2.2 40nm x 40nm x 50nm Au Cubes

The second phase of simulations involved gold nanocubes with dimensions of 40nm x 40nm x 50nm, arranged with a 5nm separation. To enhance the precision of the results, the upper boundary of the lower cube and the lower boundary of the cube positioned 5nm above were meticulously fine-meshed. Conversely, the remaining boundaries were subjected to normal mesh settings, given their minimal impact on calculating the generalized flux. Employing uniform meshing for both cubes aimed at streamlining the simulation process and facilitating analytical method solutions. A gradual mesh element growth rate of 1.1 was employed to ensure smooth transitions between fine and normal mesh regions. The meshing procedures were conducted using COMSOL, and the subsequent SCUFF-NEQ simulations were executed on the Alpine Supercomputer. The dielectric function was given by $\epsilon(\omega) = \frac{(1-\omega_p^2)}{\omega(\omega+i\Gamma)}$ where ω_p=1.37 x 10^{16} and Γ=5.32 x 10^{13} Similar to the initial simulation, the surface plasmon resonance of the 40nm x 40nm x 50nm gold nanocubes manifested within the frequency range of 0.2 x 3e14 rad/sec to 0.3 x 3e14 rad/sec. This was evident through peaks observed in both analytical and simulated results, resembling those obtained in the first simulation. In the figure, the red line corresponds to the analytical solution for the generalized flux, while the black line signifies the simulated results. The alignment of peaks at identical frequencies strongly implies the accuracy of the simulated outcomes. However, disparities in the peak values of the generalized flux between the analytical and simulated results point to a tendency of analytical solutions to overestimate energy transfer between the boundaries. This discrepancy is attributed to the analytical model's oversight of escaping electromagnetic waves. This observation emphasizes the significance of considering finite size effects, particularly given the proximity of the boundary sizes to the gap between the two nanocubes. Notably, a comparative

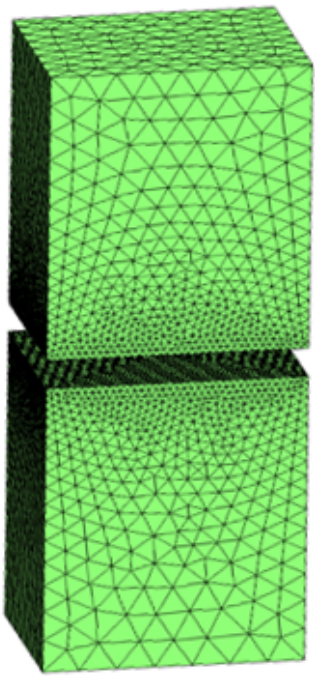

(a) Mesh geometry of 40nm x 40nm x 50nm Au Cubes with a gap of 5nm.

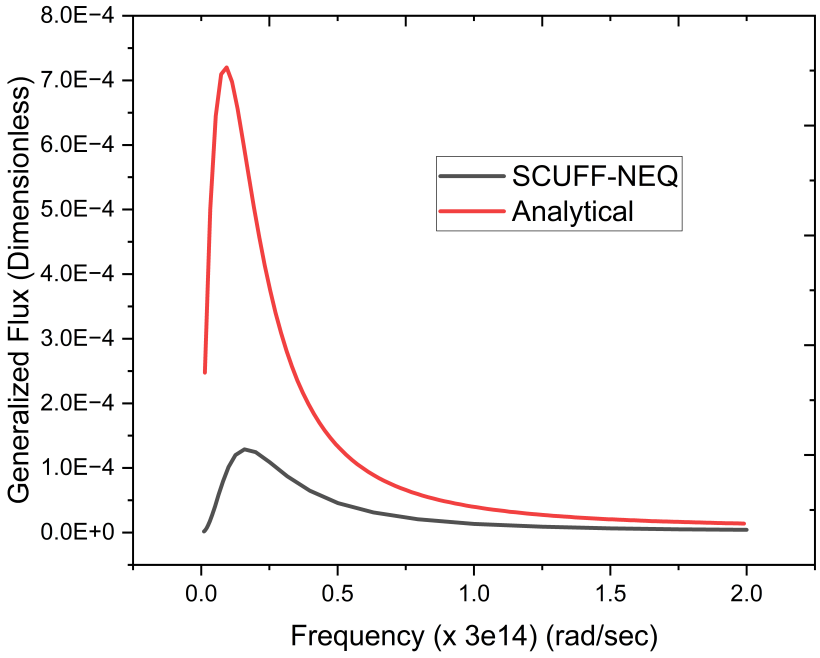

(b) Generalized Flux vs. Frequency for 40nm x 40nm x 50nm Au Cubes with a gap of 5nm.

Figure 4.4: Comparing values of generalized flux using analytical method and SCUFF-EM simulations for 40nm x 40nm x 50nm Au Cubes with a gap of 5nm.

analysis with the first simulation indicates a reduction in the difference between the analytical and simulated solutions. This reduction implies that, as the size of the gold nanocubes increases, finite size effects diminish. The diminishing effects suggest that as the size of the cubes approaches the distance of separation, the nanocubes behave similar to two infinitely large boundaries. In essence, the second simulation further reaffirms the presence of finite size effects and underscoring the importance of considering these effects in analytical models.

4.2.3 80nm x 80nm X 50nm Au Cubes

The final simulation case involved 80nm x 80nm x 50nm gold nanocubes separated by 5nm, maintaining a mesh geometry similar to the preceding two cases. In contrast to the earlier scenarios, this model exhibited a notable convergence between analytical and simulated results for the generalized flux. This agreement can be attributed to the larger size of the cube boundaries, which, when compared to the separation distance between the objects, allows them to be considered as semi-infinite. Consequently, this case elucidates the diminishing effects of finite size. The dielectric function was given by $\epsilon(\omega) = \frac{\left(1-\omega_p^2\right)}{\omega(\omega+i\Gamma)}$ where ω_p=1.37 x 10^{16} and Γ=5.32 x 10^{13} In parallel with the preceding cases, the surface plasmon resonance of the 80nm x 80nm x 50nm gold nanocubes manifested within the frequency range of 0.2 x 3e14 rad/sec to 0.3 x 3e14 rad/sec. This manifestation was evident through observed peaks in both analytical and simulated results, akin to those obtained in the initial simulation. In the graphical representation, the red line corresponds to the analytical solution for the generalized flux, while the black line signifies the simulated results. The alignment of peaks at identical frequencies strongly suggests the accuracy of the simulated outcomes. The third case serves as a pivotal illustration of the diminishing effects of finite size, with the larger cube boundaries allowing for a close agreement between analytical and simulated results. This finding contributes to a nuanced understanding of the interplay between boundary size and separation distance in near field heat transfer solution, emphasizing the importance of considering these factors in near field analyses.

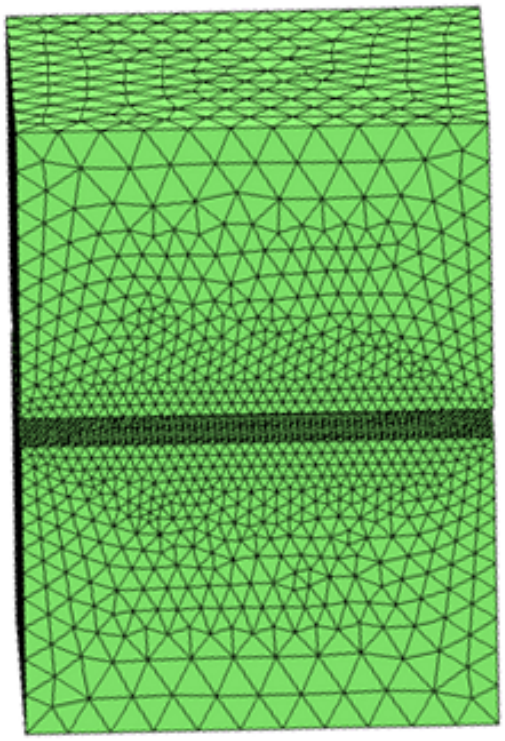

(a) Mesh geometry of 80nm x 80nm x 50nm Au Cubes with a gap of 5nm.

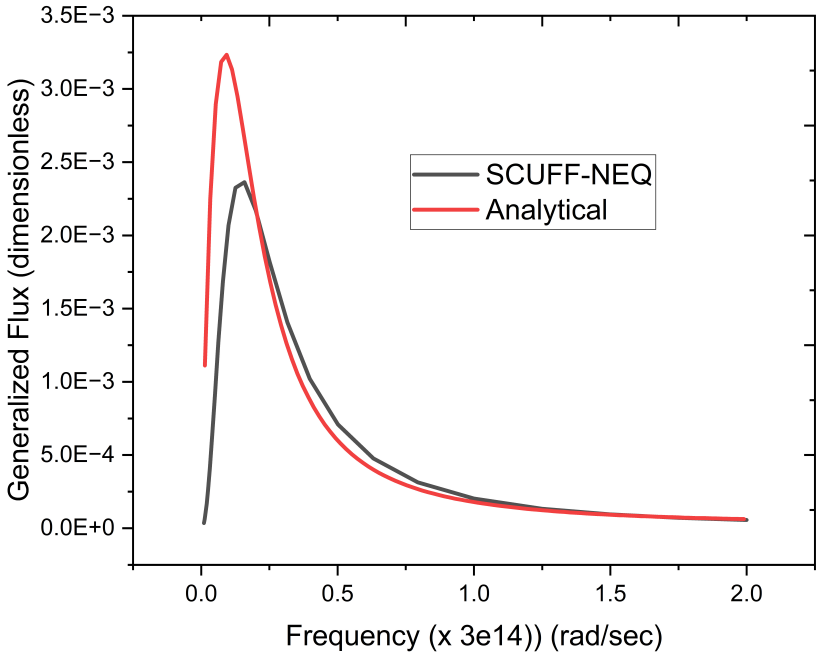

(b) Generalized Flux vs. Frequency for 80nm x 80nm x 50nm Au Cubes with a gap of 5nm.

Figure 4.5: Comparing values of generalized flux using analytical method and SCUFF-EM simulations for 80nm x 80nm x 50nm Au Cubes with a gap of 5nm.

4.2.4 Lateral Size Effects

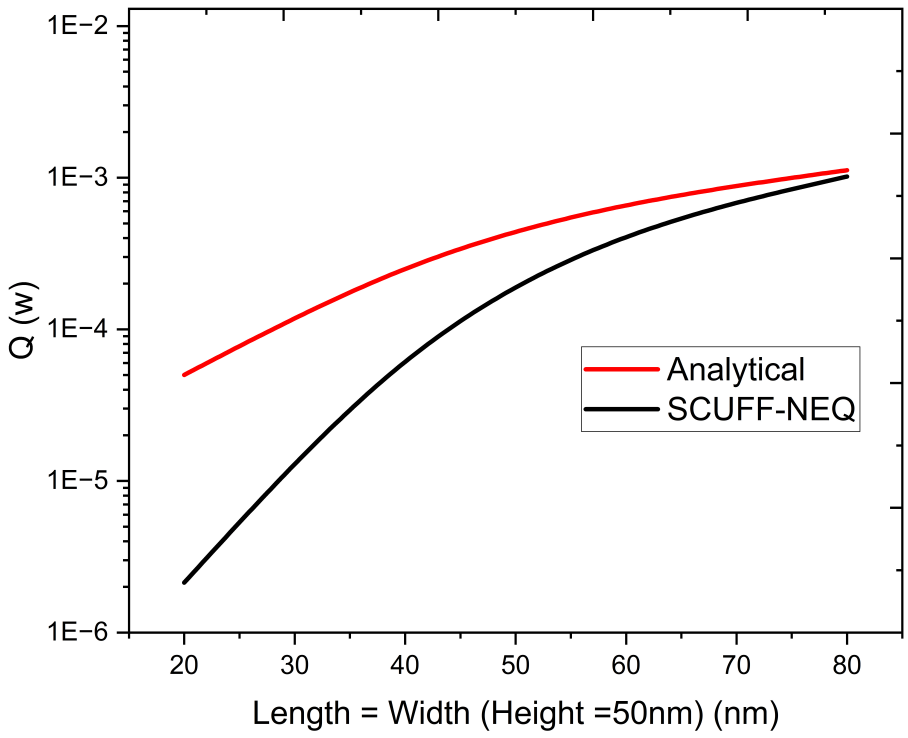

Figure 4.6: Computed radiative heat flux between two cubes as a function of changing lateral dimesions. (Length = Width, Height = 50nm)

In summary, a series of simulations were conducted to examine near-field heat transfer using gold nanocubes of varying sizes. The initial simulation involved 20nm x 20nm x 50nm cubes with a 5nm separation, revealing surface plasmon resonance in the frequency range of 0.2 x 3e14 rad/sec to 0.3 x 3e14 rad/sec. Discrepancies in peak values indicated finite size effects and the oversight of escaping electromagnetic waves in analytical models. Subsequent simulations with larger cubes (40nm x 40nm x 50nm and 80nm x 80nm x 50nm) and similar separations showed a diminishing difference between analytical and simulated outcomes, suggesting reduced finite size effects as cube size increased. The final simulation with the largest cubes demonstrated signif-

icant convergence between analytical and simulated results, attributed to the larger size of cube boundaries. Throughout all simulations, the resonance peak in generalized flux occurred within the same frequency range, highlighting the accuracy of simulated outcomes. The study underscored the importance of considering finite size effects and the effects of boundary size in near-field heat transfer analyses. By substituting obtained generalized flux values into equation 3.5 from chapter 3, the near-field radiative heat flux between the cubes was calculated for all three cases. The heat flux values were then plotted against the respective length and width. The convergence of heat flux values was observed as the length and width of the cubes increased, indicating a transition to behavior akin to semi-infinite boundaries compared to the gap size.

4.3 Simulated vs Analytical Results for Changing Gap Size

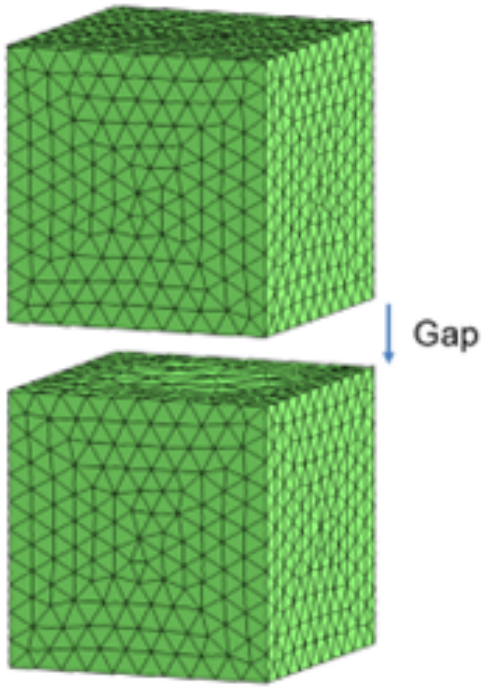

Figure 4.7: Visualization of changing gap size between two cube geometries.

After examining the impact of cube dimensions on near-field radiative heat transfer, the

subsequent investigation focused on the influence of gap size. In this scenario, the dimensions of the cubes were maintained at 50nm x 50nm x 50nm, while the distance between the top and bottom cubes varied from 1nm to 80nm. Five test cases were considered with gap sizes of 1nm, 5nm, 20nm, 40nm, and 80nm. The boundaries facing each other underwent fine meshing, while the remaining boundaries on both cubes were meshed using normal settings in COMSOL. To ensure a smooth transition between regions of finer and coarser mesh, a gradual element growth rate of 1.1 was employed.The dielectric function for Au (gold) was given by $\epsilon(\omega) = \frac{(1-\omega_p^2)}{\omega(\omega+i\Gamma)}$ where ω_p=1.37 x 10^{16} and Γ=5.32 x 10^{13} The initial simulation involved a 50nm x 50nm x 50nm cube with a 1nm gap size. Subsequent simulations were studied for growing gap sizes. The surface plasmon resonance fell within the range of 0.2 x 3e14 rad/sec to 0.3 x 3e14 rad/sec, consistent with our previous findings as evident by the peaks of generalized flux in our results. Although there was not complete convergence between the analytical and simulated results, subsequent simulations indicated that the disparity increased as the gap size expanded. This observation suggests that finite size effects become more pronounced with larger gap sizes.

4.3.1 Gap Size of 1nm

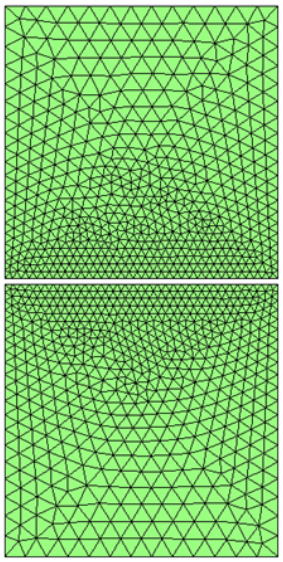

(a) Mesh geometry of 50nm x 50nm x 50nm Au Cubes with a gap of 1nm.

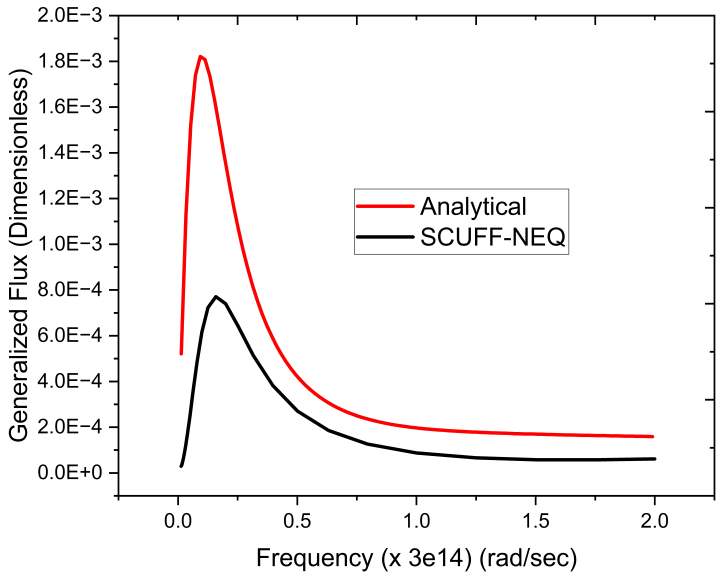

(b) Generalized Flux vs. Frequency for 50nm x 50nm x 50nm Au Cubes with a gap of 1nm.

Figure 4.8: Comparing values of generalized flux using analytical method and SCUFF-EM simulations for 50nm x 50nm x 50nm Au Cubes with a gap of 1nm.

4.3.2 Gap Size of 5nm

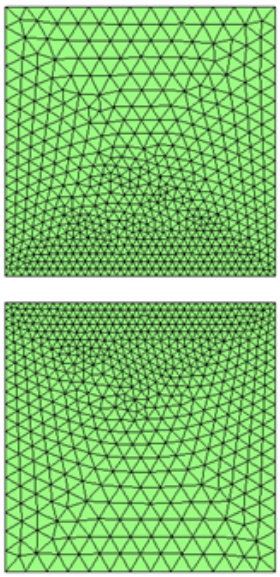

(a) Mesh geometry of 50nm x 50nm x 50nm Au Cubes with a gap of 5nm.

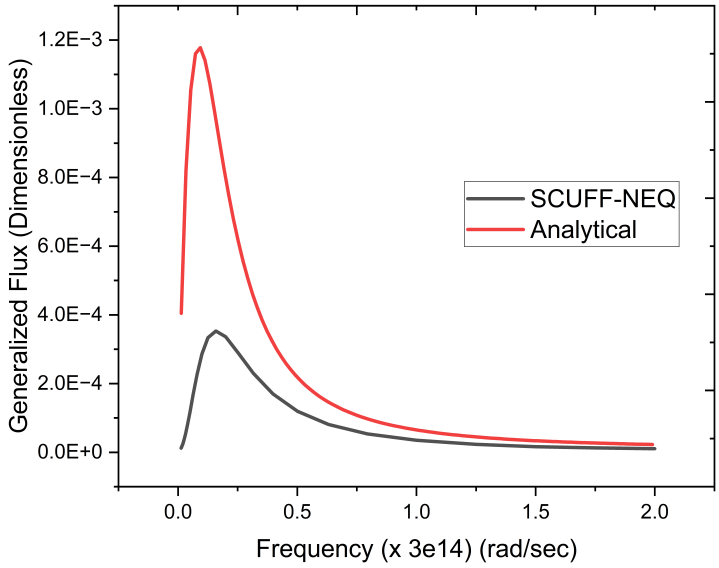

(b) Generalized Flux vs. Frequency for 50nm x 50nm x 50nm Au Cubes with a gap of 1nm.

Figure 4.9: Comparing values of generalized flux using analytical method and SCUFF-EM simulations for 50nm x 50nm x 50nm Au Cubes with a gap of 5nm.

4.3.3 Gap Size of 20nm

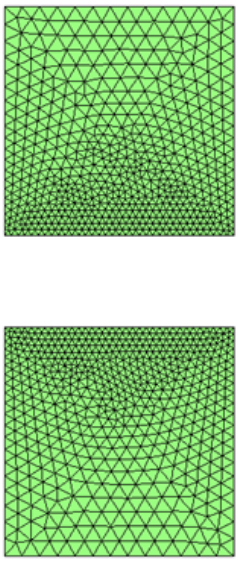

(a) Mesh geometry of 50nm x 50nm x 50nm Au Cubes with a gap of 20nm.

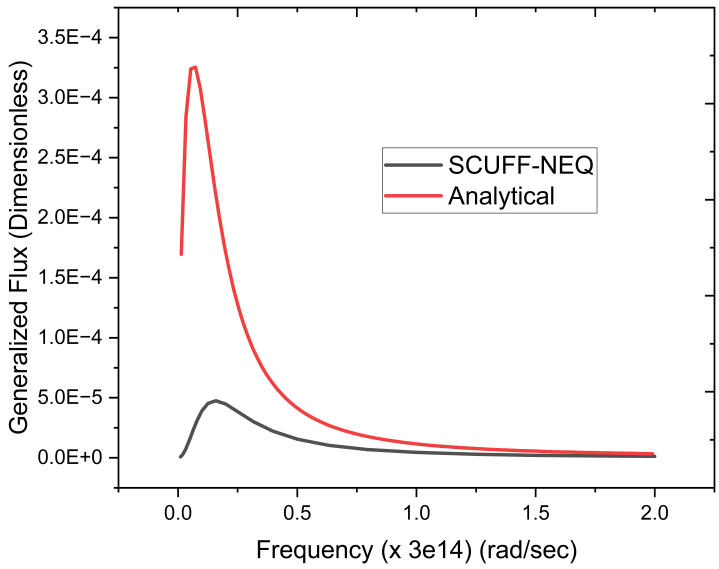

(b) Generalized Flux vs. Frequency for 50nm x 50nm x 50nm Au Cubes with a gap of 20nm.

Figure 4.10: Comparing values of generalized flux using analytical method and SCUFF-EM simulations for 50nm x 50nm x 50nm Au Cubes with a gap of 20nm.

4.3.4 Gap Size of 40nm

(a) Mesh geometry of 50nm x 50nm x 50nm Au Cubes with a gap of 40nm.

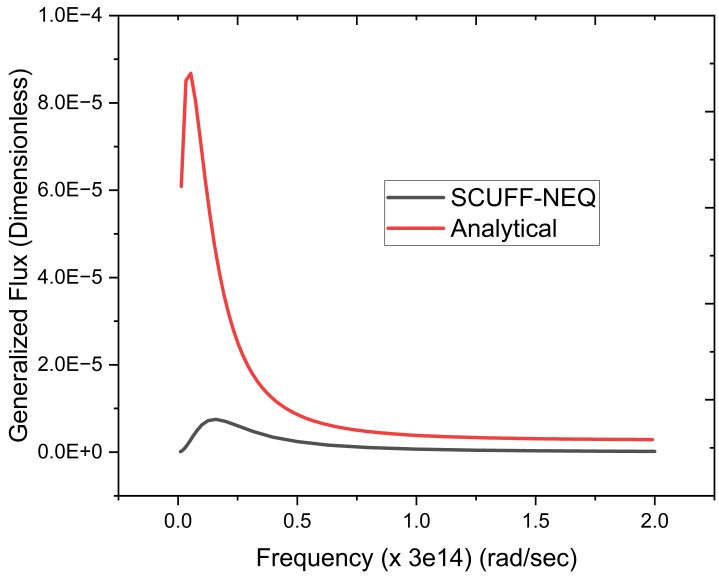

(b) Generalized Flux vs. Frequency for 50nm x 50nm x 50nm Au Cubes with a gap of 40nm.

Figure 4.11: Comparing values of generalized flux using analytical method and SCUFF-EM simulations for 50nm x 50nm x 50nm Au Cubes with a gap of 40nm.

4.3.5 Gap Size of 80nm

(a) Mesh geometry of 50nm x 50nm x 50nm Au Cubes with a gap of 80nm.

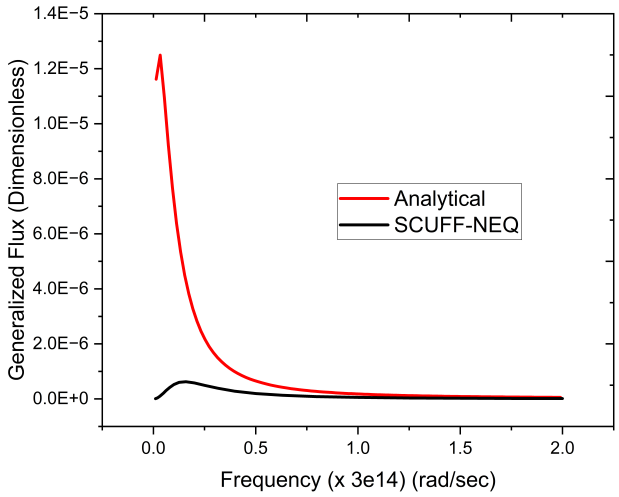

(b) Generalized Flux vs. Frequency for 50nm x 50nm x 50nm Au Cubes with a gap of 80nm.

Figure 4.12: Comparing values of generalized flux using analytical method and SCUFF-EM simulations for 50nm x 50nm x 50nm Au Cubes with a gap of 80nm.

4.3.6 Gap Size Effects

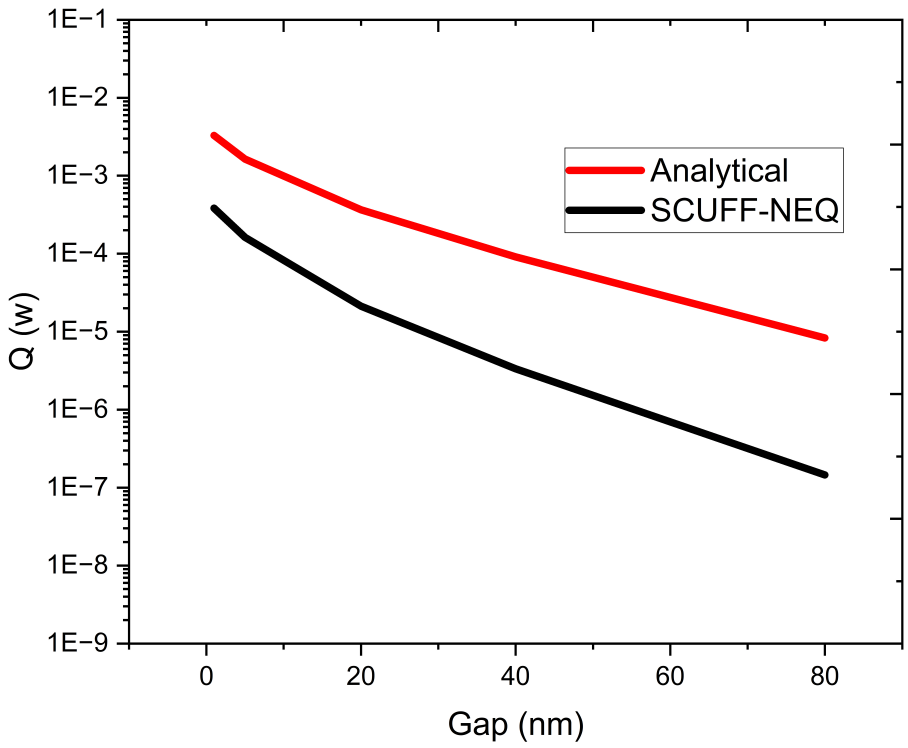

Figure 4.13: Computed radiative heat flux between two cubes as a function of changing gap dimesions. (Length = Width = Height = 50nm)

A sequence of simulations was conducted to investigate near-field heat transfer using gold nanocubes with varying gaps between them. In the initial simulation, 50nm x 50nm x 50nm cubes with a 1nm separation exhibited surface plasmon resonance within the frequency range of 0.2 x 3e14 rad/sec to 0.3 x 3e14 rad/sec. The findings from this case indicated that for smaller gap sizes, the boundaries facing each other behaved like semi-infinite surfaces, as their dimensions were significantly larger than the gap size, resulting in a diminishing finite size effect.

Subsequent simulations with larger gap sizes (5nm, 20nm, 40nm, and 80nm) while maintaining similar cube sizes revealed an increasing disparity between analytical and simulated outcomes.

This suggested an amplified impact of finite size effects as the gap size expanded. In the final simulation with the largest gap of 80nm, a noteworthy divergence between analytical and simulated results was observed, attributed to the substantial gap size between cube boundaries.

Throughout all simulations, the resonance peak in generalized flux consistently occurred within the same frequency range, affirming the precision of simulated outcomes. The study emphasized the significance of considering finite size effects and the interplay of separation distance in near-field heat transfer analyses. By inserting the obtained generalized flux values into equation 3.5 from Chapter 3, the near-field radiative heat flux between the cubes was computed for all five cases. The resulting heat flux values were then plotted against the respective gap size. The convergence of heat flux values was evident as the gap size decreased, indicating a shift towards behavior resembling semi-infinite boundaries relative to the gap size.

Chapter 5

Conclusion

To conclude our work revolves around uncovering and illustrating the significant impact of finite size effects in the realm of near field radiative heat transfer. Our simulations yielded crucial insights, demonstrating how these effects evolve concerning varying dimensions and gap sizes within cube structures.

One of the pivotal findings of our study pertains to the relationship between finite size effects and the dimensions of the cubes. Our simulations vividly showcased that as the dimensions of the cubes increase while maintaining a consistent gap size, the influence of finite size effects gradually diminishes. This crucial observation highlights an inverse correlation between the size of the cubes and the prevalence of these effects. It underscores the pivotal role that larger dimensions play in mitigating the impact of finite size effects on near field heat transfer, potentially offering a pathway toward more predictable outcomes in experimental setups.

Similarly, our simulations unveiled another pivotal insight regarding the interplay between finite size effects and gap sizes. When keeping the dimensions of the cubes constant and reducing the gap sizes, our findings unmistakably demonstrated a concurrent reduction in the influence of finite size effects. This discovery underscores the importance of gap size in modulating the impact of these effects. Decreasing the gap size emerges as a key factor in diminishing the prevalence of finite size effects, suggesting its significance as a design consideration in experimental setups aimed at accurately predicting near field heat flux.

The implications of these revelations extend far beyond the confines of theoretical simulations.

Understanding the behavior of finite size effects concerning cube dimensions and gap sizes holds profound significance in guiding and shaping future experimental endeavors. Our findings serve as a guide, illuminating the path for researchers and engineers engaged in experimental work aimed at predicting near field heat flux accurately.

In the pursuit of precision and reliability in experimental setups, our research highlights the criticality of considering cube dimensions and gap sizes. Armed with the knowledge of how these parameters interplay with finite size effects, researchers can now make informed decisions when designing and conducting experiments related to near field radiative heat transfer.

This newfound understanding not only enriches the theoretical framework but also bears immense practical implications. It empowers experimentalists to tailor their setups intelligently, enhancing the accuracy and reliability of predictions regarding near field heat transfer. As a result, future advancements and innovations in this domain stand to benefit immensely from the foundational insights provided by our work.

Bibliography

[1] S. Basu, Z. M. Zhang, and C. J. Fu, "Review of near-field thermal radiation and its application to energy conversion," International Journal of Energy Research, vol. 33, no. 13, pp. 1203–1232, 2009.

[2] K. Nguyen, O. Merchiers, and P.-O. Chapuis, "Near-field radiative heat transfer in scanning thermal microscopy computed with the boundary element method," Journal of Quantitative Spectroscopy and Radiative Transfer, vol. 202, pp. 154–167, 2017.

[3] R. Siegel, Thermal Radiation Heat Transfer, Fourth Edition. Taylor & Francis, 2001.

[4] Z. M. Zhang, Nonequilibrium Energy Transfer in Nanostructures, pp. 345–405. Cham: Springer International Publishing, 2020.

[5] S. Rytov, I. Kravtsov, and V. Tatarski, Principles of Statistical Radiophysics. No. v. 3 in Plasmas; 5, Springer-Verlag, 1987.

[6] J. B. Pendry, "Radiative exchange of heat between nanostructures," Journal of Physics: Condensed Matter, vol. 11, p. 6621, sep 1999.

[7] J.-P. Mulet, K. Joulain, R. Carminati, and J.-J. Greffet, "Enhanced radiative heat transfer at nanometric distances," Microscale Thermophysical Engineering - MICROSCALE THERMOPHYS ENG, vol. 6, pp. 209–222, 07 2002.

[8] J.-P. Mulet, K. Joulain, R. Carminati, and J.-J. Greffet, "Nanoscale radiative heat transfer between a small particle and a plane surface," Applied Physics Letters, vol. 78, pp. 2931–2933, 05 2001.

[9] A. W. Rodriguez, M. T. H. Reid, and S. G. Johnson, "Fluctuating-surface-current formulation of radiative heat transfer for arbitrary geometries," Phys. Rev. B, vol. 86, p. 220302, Dec 2012.

[10] D. Griffiths, Introduction to Electrodynamics. Prentice Hall, 1999.

[11] S. Basu, Near-Field Radiative Heat Transfer across Nanometer Vacuum Gaps: Fundamentals and Applications. 06 2016.

[12] E. G. Cravalho, C. L. Tien, and R. P. Caren, "Effect of Small Spacings on Radiative Transfer Between Two Dielectrics," Journal of Heat Transfer, vol. 89, pp. 351–358, 11 1967.

[13] M. T. Homer Reid and S. G. Johnson, "Efficient Computation of Power, Force, and Torque in BEM Scattering Calculations," ArXiv e-prints, July 2013.

[14] J. T. Katsikadelis, "Chapter one - introduction," in The Boundary Element Method for Engineers and Scientists (Second Edition) (J. T. Katsikadelis, ed.), pp. 1–12, Oxford: Academic Press, second edition ed., 2016.

Appendix A

MATLAB Code for Analytical Solutions

Listing A.1: This is the MATLAB code used for analytical results.

```
Sclear all
clc

temp(1)=301;
temp(3)=300;
c=2.998e8;  %m/s
h_bar=6.6252e-34/2/pi;
k_b=1.38e-23;
d=10*1e-9;

w_min=1;
w_max=4e14;
number_mesh_w=100;
delta_w=(w_max-w_min)/number_mesh_w;
qq_s=0;
qq_p=0;
for y=1:number_mesh_w
    progress=y/number_mesh_w*100
w=w_min+(y-0.5)*delta_w;
frequency(y)=w;
beta_min=1;
beta_max=1e10;   %18/3*1e8~~5.3e8, so we consider one order higher value!
number_mesh_beta=64000;
delta_beta=(beta_max-beta_min)/number_mesh_beta;
ss_s=0;
```

```
ss_p=0;
for f=1:number_mesh_beta

beta=beta_min+(f-0.5)*delta_beta;

for j=1:3
    el_fun(j)=drude_n_type(w);
    el_fun(2)=1;
    k(j)=el_fun(j)^0.5*w/c;
    gama(j)=(k(j)^2-beta^2)^0.5;
end

for j=1:2:3
    r_s(2,j)=(gama(2)-gama(j))/(gama(2)+gama(j));
    ro_s(2,j)=abs(r_s(2,j))^2;
    r_p(2,j)=(el_fun(j)*gama(2)-gama(j))/(el_fun(j)*gama(2)+gama(j));
    ro_p(2,j)=abs(r_p(2,j))^2;
end

if beta<w/c
    s_prop_s= beta/4*(1-ro_s(2,1))*(1-ro_s(2,3))/abs(1-r_s(2,1)*r_s(2,3)*exp(2j*gama(2)*d))
        ^2;
    s_prop_p= beta/4*(1-ro_p(2,1))*(1-ro_p(2,3))/abs(1-r_p(2,1)*r_p(2,3)*exp(2j*gama(2)*d))
        ^2;
    s_s= s_prop_s;
    s_p= s_prop_p;
else
    s_evan_s= imag(r_s(2,1))*imag(r_s(2,3))*beta*exp(-2*imag(gama(2))*d)/abs(1-r_s(2,1)*r_s
        (2,3)*exp(-2*imag(gama(2))*d))^2;
    s_evan_p= imag(r_p(2,1))*imag(r_p(2,3))*beta*exp(-2*imag(gama(2))*d)/abs(1-r_p(2,1)*r_p
        (2,3)*exp(-2*imag(gama(2))*d))^2;
    s_s= s_evan_s;
    s_p= s_evan_p;
end

ss_s=ss_s+s_s*delta_beta;
ss_p=ss_p+s_p*delta_beta;
end
```

```
for j=1:2:3
    teta(j)=h_bar*w/(exp(h_bar*w/k_b/temp(j))-1);
end

q_s=1/pi^2*(teta(1)-teta(3))*ss_s;
flux_w_s(y)=q_s;
q_p=1/pi^2*(teta(1)-teta(3))*ss_p;
flux_w_p(y)=q_p;
flux_w(y)=q_s+q_p;
qq_s=qq_s+q_s*delta_w;
qq_p=qq_p+q_p*delta_w;
qq=qq_s+qq_p;
meher(y)=qq/(1*(Teta_temp_source-Teta_temp_reciever))*C_area;
end

plot(frequency, meher)
```